

Chapter 3

Verification

3.0 Concept and literature review

The increasing demand of CFD numerical codes in various scientific and engineering fields calls for methods to establish the accuracy of the numerical scheme. With increases in computational power, CFD practitioners often focus on solving more complex and difficult problems rather than demonstrating the accuracy of their current problems which can lead to a decrease in the quality of their simulations. Previous works on verification and validation in the CFD community [1-6] define verification as demonstrating the mathematical correctness of the numerical simulation. This usually means that if the observed discretization error decreases to zero as the mesh increments decrease to zero, then the equations are “solved correctly”. In other words, code verification is a procedure to demonstrate that the governing equations, as implemented in the code, are solved consistently.

Verification of CFD codes has been the subject of many studies in recent years. Abanto et al [3] demonstrated an approach to test the accuracy of some of the most widespread commercial codes. They presented grid convergence studies on atypical CFD cases using some commercial CFD packages. Their verification test cases include an incompressible laminar Poiseuille flow, a manufactured incompressible laminar boundary layer flow, an incompressible re-circulating flow and an incompressible annular flow. Different types of structured and unstructured meshes were used during the study. They observed non-monotonic grid convergence for all their test cases. Iterative convergence of the discrete equations to machine zero did not guaranty accurate flow field predications which meant that the codes converged to wrong solutions. From their study, they recommended that users perform the

verification of commercial CFD codes and be cautious when using the commercial codes on industrial problems.

Kleb and Wood [4] pointed out that the computational simulation community is not routinely publishing independently verifiable tests to accompany new models or algorithms. They mentioned the importance of conducting component-level verification tests before attempting system-level verification and also publishing them when introducing a new component algorithm. They proposed a protocol for the introduction of new methods and physical models that would provide the computational community with a credible history of documented, repeatable verification tests that would enable independent replication.

Roache [1, 5] discussed the verification of codes and calculations along with some definitions and descriptions related to confidence building in computational fluid dynamics. Verification was described as solving the equations right and validation as solving the right equations. Different aspects discussed in the paper include the distinction between code verification and validation, grid convergence and iterative convergence, truncation error and discretization error. Also discussed were verification of calculations, error taxonomies, code verification via systematic grid convergence testing, the Grid Convergence Index (GCI) and sensitivity of grid convergence testing. According to the author, verification does not include all aspects of code quality assurance like the important concerns of version control or archiving of input data. In the book by Roache et al [5], the authors comprehensively discussed code verification, the Method of Manufactured Solutions (MMS) used to obtain exact solutions for code verification purposes, and order of accuracy verification. A more recent study of code verification conducted by Shunn et al [6] demonstrates the MMS verification technique as applied to variable density solvers. In this study, verification was used to investigate the effects

of tabulated state-equations and temporal iteration errors on the convergence and accuracy of the code. The two problems constructed were diffusive mixing of species, and convection of density fronts which reflect basic physical phenomena found in combustion problems. The grid refinement studies that were performed confirm the spatial convergence rate of solver to be second order when an analytical equation of state (EOS) is used. Convergence of the flow variables to the exact solution were found to be impaired when the EOS was linearly interpolated in space. It was also found that EOS interpolation errors introduce spurious numerical fluctuations in the flow variables, with velocity and pressure being particularly vulnerable. This particular variable density algorithm showed first order temporal evolution of the flow when a single outer density iteration was applied. Temporal errors were generally not dominant when multiple outer density iterations were performed, making it difficult to confirm the temporal accuracy of the method with multiple outer iterations.

3.1 Verification procedures

The intent of this chapter is to present a suitable verification framework that can be applied to our own in-house solver, `les3d-mp`. The procedure can be used to provide a pass-fail acceptance criteria commonly used in the community to establish the validity of CFD solvers [6]. This same procedure is found to be very helpful in detecting coding mistakes (bugs) that are associated with spatial or temporal discretization of the transport equations. The need for verification in this project arises due to the introduction of numerical schemes and models to account for variable density Low-Mach number physics. Numerical schemes and model developments were presented in Chapter 2.

Currently, our verification procedure consists of comparing our computational solution to an exact analytical solution representative of the physics involved in low-mach number problems. Comparing to an exact solution is called MES, or method of exact solutions, and is a

powerful verification technique when one can develop an analytical solution for a test case. Comparing to an exact solution brings up the notion of discretization errors which are inherent to any solver that discretizes a set of governing PDEs into a finite dimensional subspace which approximates the continuum solution. The difference between the two is the discretization error. Discretization methods are *consistent* if the error goes to zero as the representative cell size, h , decreases to zero (for mesh size h , then a consistent method will result in error that is proportional to h^p). The rate at which the error decreases to zero is called the order of accuracy. A discretization method is said to be second order accurate in space if the discretization error goes to zero as h^2 . According to the community the most rigorous acceptance criterion is verification of order of accuracy, in which one not only seeks to verify that the method is consistent, but also establishes the value of p and is then compared to the theoretical order of the discretization method. This is our established procedure.

The following sections present spatial and temporal order of accuracy test cases that have been developed with variable density transport equations in mind. The first part presents cases related to the spatial order of accuracy where we seek to establish the second order accuracy of les3d-mp through a one dimensional isothermal binary mixing case where large density ratios are present. We then seek to show the order of accuracy of the integration scheme options through the solution of a time dependent ODE, $u = f(t)$. Then, a time-periodic Poiseuille flow is also presented to demonstrate the order of accuracy when $u = f(u, t)$. Lastly, two classical test cases corresponding to momentum driven and buoyancy driven boundary layers are presented. Velocity, temperature and near wall property comparisons are made with the analytical Blasius and Ostrach similarity solutions. It is shown that the use of outflow boundary conditions for buoyancy driven boundary layers is not as accurate as for momentum driven boundary layers and the problem is discussed.

3.2 Spatial accuracy case

3.2.1. Isothermal Binary Mixing

The following verification case tests the ability of the solver to handle flows with large density ratios similar to those found in fires or in combustion systems. An exact solution to the one dimensional mixing of two fluids with different molecular weights is presented. The mixing occurs at constant temperature and pressure conditions. The configuration corresponds to a stratified fluid with the heavier density on top and gradually decreasing in magnitude towards the bottom of the domain (note that the configuration has zero gravity). The domain is assumed to be very large in width and depth consistent with using periodic conditions in streamwise and spanwise direction. The restriction of no-slip boundary flow is imposed at the bottom of the domain. This is shown in the following figure,

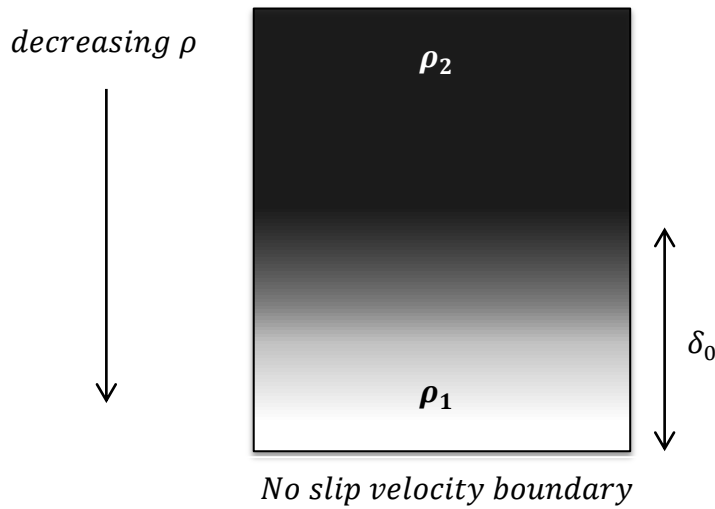


Figure 1. 1D binary mixing schematic. Initial mixing layer thickness is shown by δ_0

3.2.1.1 Governing Equations

An exact solution for the binary mixing problem is found for the density field which directly couples the mixture fraction and velocity. The solution has the characteristic of being a transient mass-density diffusion equation satisfying, $\frac{\partial \rho}{\partial t} = D \frac{\partial^2 \rho}{\partial y^2}$. The density field solution has the following form:

$$\rho(y, t) = \rho_2 + (\rho_1 - \rho_2) \frac{\delta_0}{\sqrt{4\pi D(t + t_0)}} e^{\frac{-y^2}{4D(t+t_0)}}$$

Where the density values are assigned through molecular weights of heavy and light fluids through an equation of state (EOS) and δ_0 represents a characteristic mixing length scale. The mixture fraction field for the first scalar is now defined as,

$$Z(y, t) = \frac{\frac{1}{\rho(y, t)} - \frac{1}{\rho_2}}{\frac{1}{\rho_1} - \frac{1}{\rho_2}}$$

Using the one-dimensional continuity equation with transient and lateral velocity terms gives the vertical component of velocity as,

$$v(y, t) = \frac{(\rho_1 - \rho_2)}{\rho(y, t)} \frac{\delta_0}{\sqrt{4\pi D(t + t_0)}} \left(\frac{y}{2(t + t_0)} \right) e^{\frac{-y^2}{4D(t+t_0)}}$$

It should be noted that all the above solutions have a singularity at time ($t=0$), thus an offset time, t_0 , is added based on diffusion time scales to avoid an unphysical solution. The analysis of this problem begins at $t_0=10$. Also note that the reference density fields corresponding to isothermal light and heavy fluid mixing in air (ρ_1, ρ_2) are defined through the use of the equation of state (Table 1). The species fraction of oxygen and nitrogen in air are: $Y_{O_{2air}} = 0.233$ and $Y_{N_{2air}} = 1 - Y_{O_{2air}}$, they are used calculate the molecular weight of the mixture composition,

$$MW_{mix} = \frac{1}{\left(\frac{Y_{O_2}}{MW_{O_2}} + \frac{Y_{N_2}}{MW_{N_2}} \right)}$$

$$\rho_1 = \rho_{air} \frac{MW_1}{MW_{air}}$$

$$\rho_2 = \rho_{air} \frac{MW_2}{MW_{air}}$$

The verification task begins by initializing the code with the above equations at an offset time, $t_0=10$. The domain is selected as $(L_x, L_y, L_z) = (10, 30, 5)$ with double periodic conditions in L_x and L_z . Grid design procedures are followed in order to resolve the characteristic mixing layer, this has a minimum length-scale of 2 and increases to 20 by the end of the simulation. Adequate resolution will ensure to have at least 30-40 points inside the minimum mixing layer set by the initial conditions. The running time is selected based on a parametric study of density ratios (Figure 1) where a peak density ratio value was found at initial offset time ($\frac{\rho_2}{\rho_1} = 19$) and decreased exponentially to nearly 1 at an approximate time of 400 time units. The density ratio values are graphically compared to the reference density field (ρ_1) showing that a running time of $t = 200$ captures the transient dynamics of interest and that no interesting dynamics occur after 1000 time units. This is shown by the following figures where the history of peak density ratios are evaluated at the bottom of the domain.

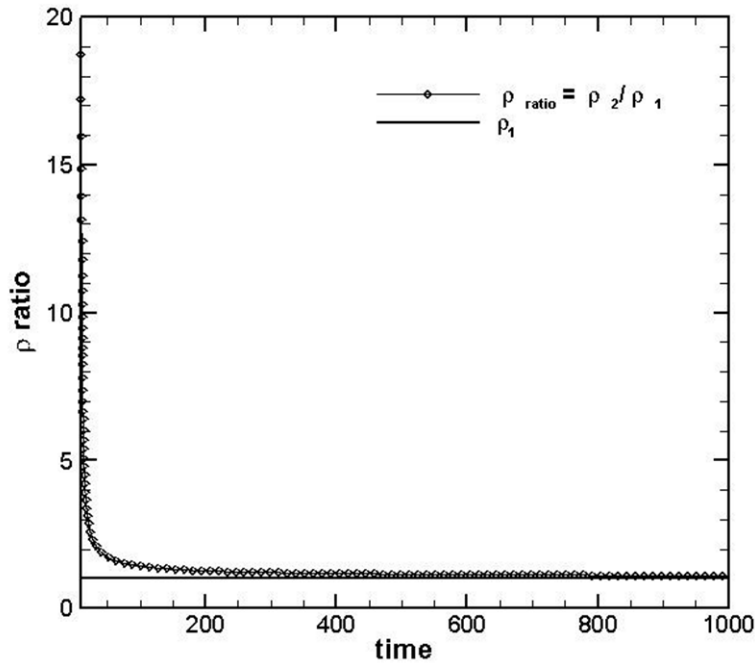


Figure 2. Time variations of minimum value of mass density in binary mixing solution.

ν_{inf}^*	Pr	MW_{mix}	ρ_1^*	ρ_2^*
0.02	0.75	$\frac{1}{\left(\frac{Y_{O_2}}{MW_{O_2}} + \frac{Y_{N_2}}{MW_{N_2}}\right)}$	$\rho_{air} \frac{MW_1}{MW_{air}} = 0.0097$	$\rho_{air} \frac{MW_2}{MW_{air}} = 1$
	t_0 (off-set time)	δ_0 (characteristic lengthscale)	Re_{ref}	$T_{inf}(K)$
	10	2	50	300

$(L_x L_y L_z)^*$	$(n_x n_y n_z)$	grid stretching
(10,30,5)	(10,1200,4) $\Delta y = 0.025$	Uniform grid in x, z, y
Initial Conditions	Specific Enthalpy model	farfield boundary
$u_{init} = 0, w_{init} = 0$ $v_{init} = v_{exact}(t = t_0)$ $Z_{init} = Z_{exact}(t = t_0)$ $h_{init} = h^*(Z_{init}, T_{inf})$	Chemkin coefficient data base w/ enthalpy polynomial: $h^* = a_6 + a_1 T + \frac{c_2 T^2}{2} + \frac{c_3 T^3}{3} + \frac{c_4 T^4}{4} + \frac{c_5 T^5}{5}$	$u_{farfield} = 0$ $\frac{dv}{dy} = 0, \frac{dw}{dy} = 0$ $\frac{dh}{dy} = 0, \frac{dZ}{dy} = 0$
wall boundary	Scalar Discretization Option	Periodicity
$u = v = w = 0$ $T_{wall} = T_{inf}$	QUICK	Spanwise, Streamwise

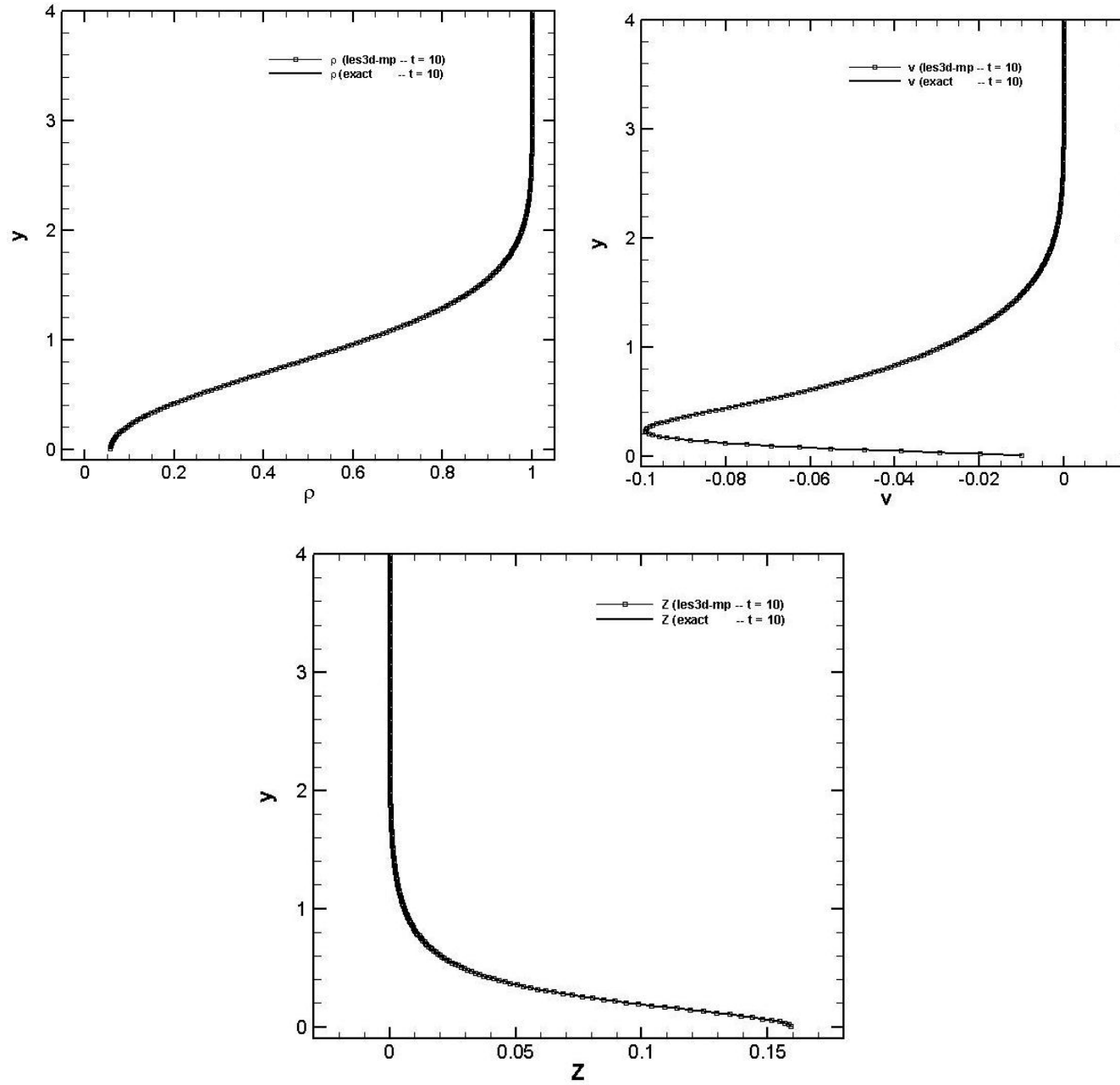
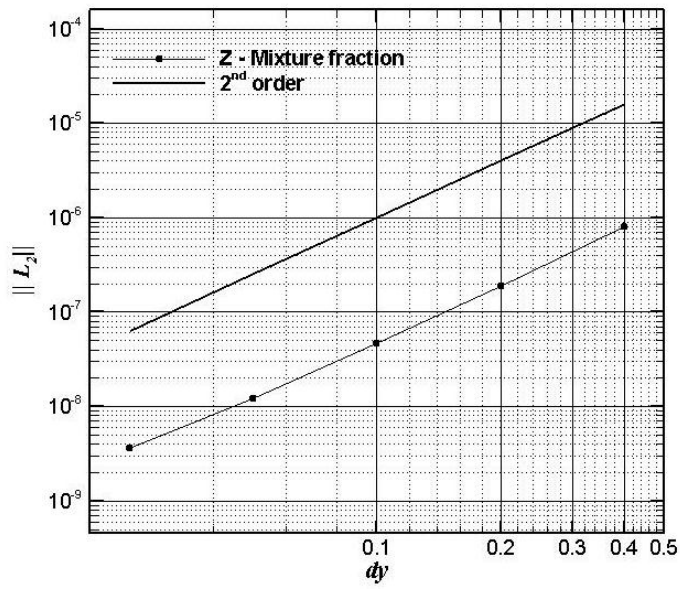
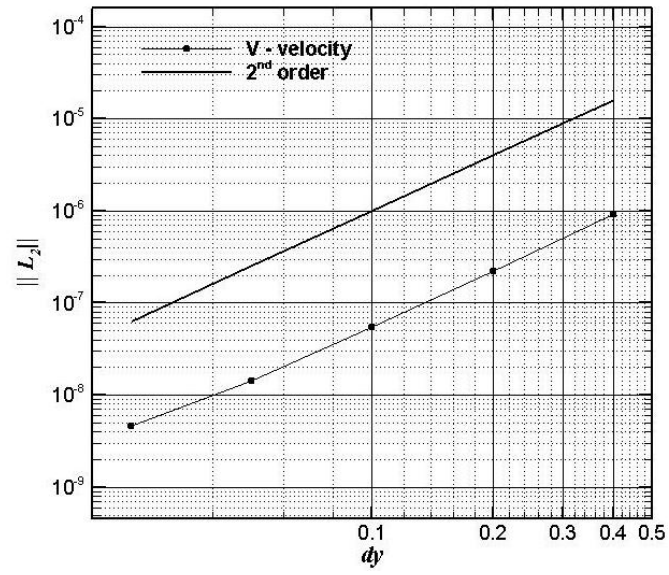
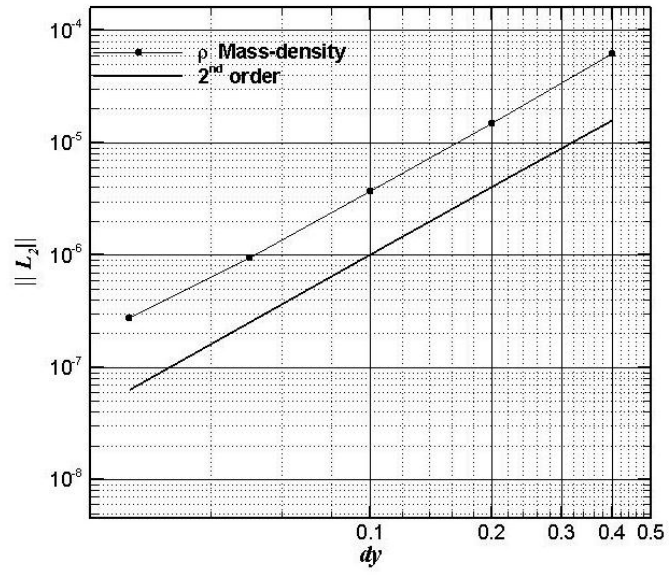


Figure 3. Mas-density, velocity and mixture fraction profiles at time $t = 10$.



3.3 Temporal accuracy cases

This section deals with showing the order of accuracy of the time integrator in les3d-mp. Two time integrating options are available, they are second order Adams-Bashford and the classical third order, low-storage Runge Kutta scheme presented in section 2. A simple transient problem strictly defined as a function of time only, $f(t)$ is selected in order to remove spatial errors from analysis. This takes the form of,

$$\frac{\partial u}{\partial t} = -\sin(\omega t)$$

Where $\omega = \frac{2\pi}{T}$ and with the following initial condition, $u(0) = 0$. Since this test case is independent of spatial variables it can be run on a very coarse computational grid, such as $(nx,ny,nz) = (4,4,4)$, or 4^3 and with a Reynolds number = 1. It makes use of periodic conditions in spanwise and streamwise directions as well as velocity symmetry conditions on the top and bottom boundaries. Symmetry conditions are defined as zero wall-normal gradients of u and w velocities and zero y -velocity at the boundaries of interest.

The velocity oscillation is introduced into les3d-mp by advancing the mean pressure gradient in time as the right hand side of the integrated solution. It is described through the mean pressure equation, $\frac{\partial \bar{P}}{\partial x} = -A \sin\left(\frac{2\pi t}{T}\right)$, where the pressure gradient amplitude, A , and the wave period, T , are given in Table 1. This transient ODE has the following analytical solution that is helpful in performing temporal order of accuracy studies,

$$u(t) = \frac{T}{2\pi} (1 + \cos(\omega t))$$

Table 1. Parameter values for transient test case.

parameter	value
T	10
A	1
Re	1
nxnynz	(4,4,4)
Periodicity	x, z

Running an order or accuracy analysis for a total running time of $3T/2$ with increasingly finer time-steps gives the results presented in figure 4 and 5. This establishes the 2nd and 3rd order accuracy of the Adams-Bashford and Runge-Kutta scheme, respectively.

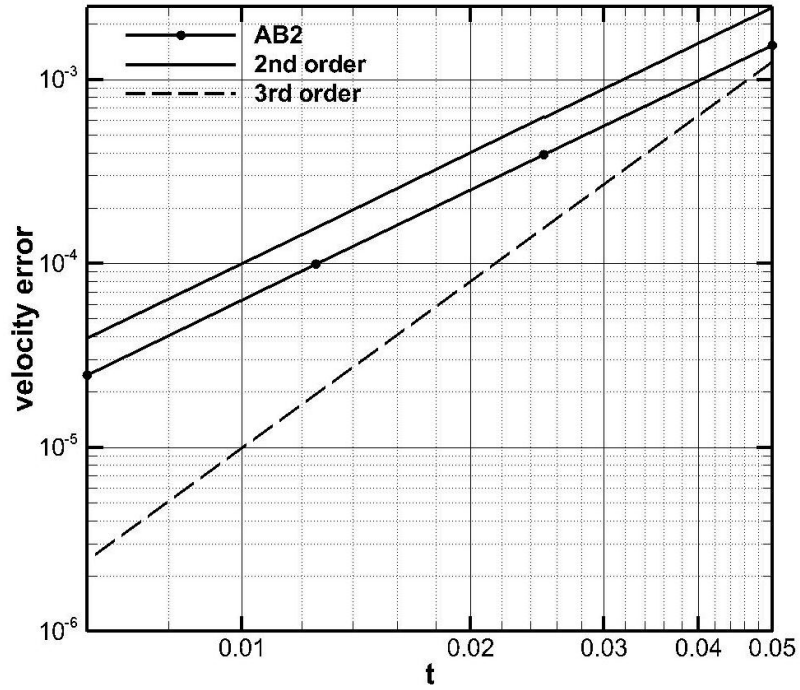


Figure 4. Order of accuracy analysis for AB2.

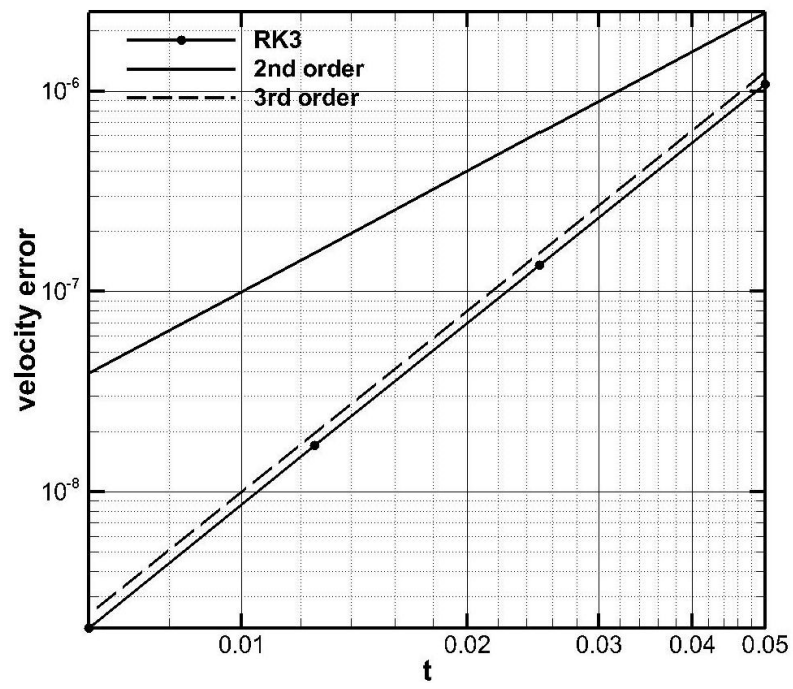


Figure 5. Order of accuracy analysis for RK3.

3.3.1 Time-Periodic Poiseuille

This section presents an order of accuracy analysis for the unsteady time-periodic Poiseuille flow. This variation of the classical flow brings in an unsteady velocity features which is specified through the pressure gradient. The unsteadiness provides regions of local acceleration/deceleration and regions of flow reversal making this an interesting academic problem. The axial pressure gradient can then be expressed, via Fourier series, in terms of sinusoidal functions of time which lead to a complete representation of velocity, pressure and shearing stress associated with this flow. The purpose of the time-periodic flow is to show the code's temporal order of accuracy when the form of the equation being solved is dependent on both temporal and spatial components, i.e., $\frac{\partial u}{\partial t} = f(u, t)$. The harmonic pressure gradient is specified as $\frac{1}{\rho} \frac{\partial p}{\partial t} = -A \exp(i\omega t)$, where ω is the standard angular frequency of the system, and A represents the amplitude. (Note the pressure gradient can also be re-written, using Euler's identity, as functions of trigonometric harmonic functions).

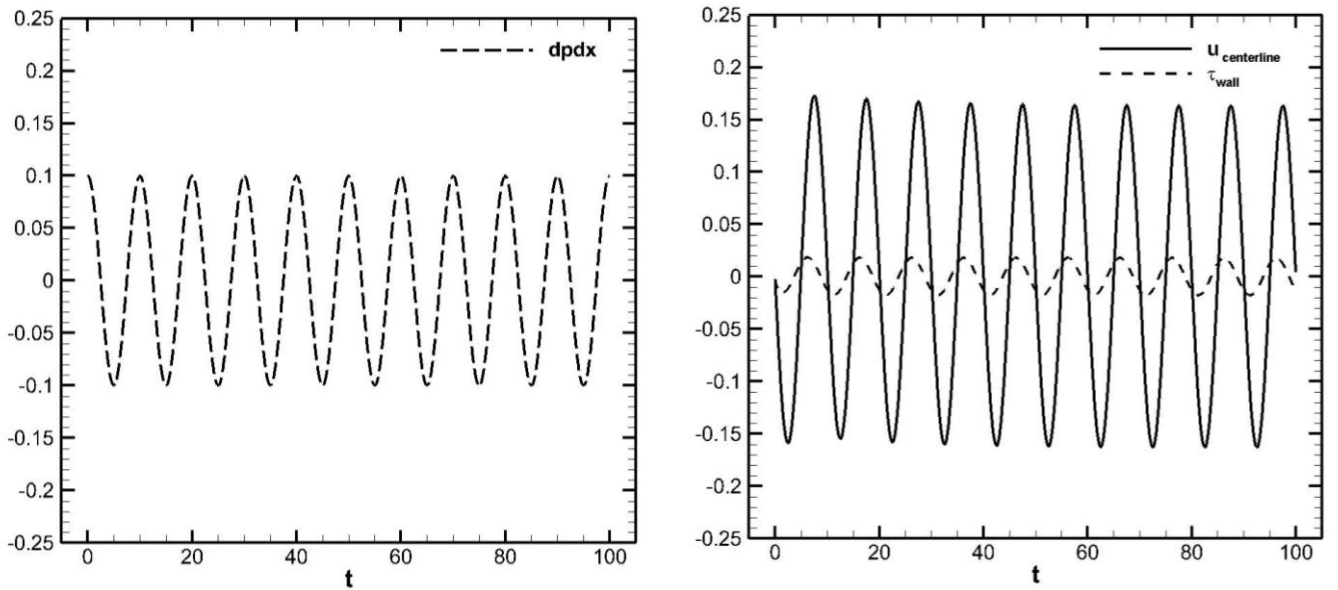


Figure 6. Time-periodic Poiseuille flow. Fourier axial pressure gradient (left), centerline velocity and wall shear stress profiles (right).

A series of finer resolution cases were studied in order to show the temporal accuracy using the error of the centerline velocity. The error was computed by comparing to a highly resolved reference solution. The results show 2nd order accuracy for the Adams-Bashford scheme.

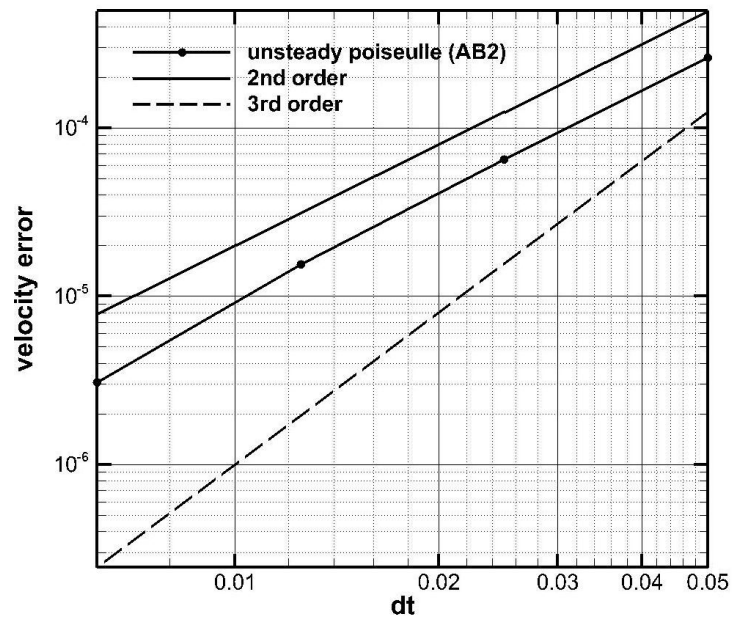


Figure 7. Order of accuracy analysis for Time-Periodic Poiseuille flow.

3.4 Classical boundary layer solutions

3.4.1 Forced convection boundary layer: Blasius Solution

We now focus our attention to modeling a Blasius flow configuration. Physically this is an important test case since it captures some of the salient features (i.e, wall shear stress, heat flux) found in momentum-driven boundary layers. Numerically this is also a challenging flow since it requires the implementation of inflow and outflow conditions to capture the spatially developing nature of the problem. The parameters necessary to implement this run are presented in Table 1 and results are shown for representative cases that correspond to the amount of heat transfer added as part of the simulation.

3.4.1.1 Results

The Blasius test cases have the following descriptions: Reynolds number of 50 with a displacement thickness and free-stream velocity of unity chosen as the reference length and velocity scales. It is performed on a computational domain of $(Lx, Ly, Lz) = (200, 60, 5.0)$ with the first grid point $\Delta y_{min} = 0.025$ and having a total of 50,000 grid cells that spatially resolve the boundary layer. Standard grid design procedures are followed ensuring that 30-40 points are used to resolve the boundary layer viscous region. This is achieved through grid stretching by means of a hyperbolic tangent function which clusters the grids near the wall. This capability allows us to be more efficient in resolving the boundary layer thickness, δ .

Testing Parameters

$\nu_{inf}(m/s^2)$	$Pr = \frac{c_p \mu}{k}$	$T_{wall}, T_{inf}(K)$	$\nu_{wall}(m/s^2)$	$k_{inf}(m/s^2)$
0.02	0.71	450, 300K	$\nu_{inf} \left(\frac{T_w}{T_a} \right)^{1.76}$ = 0.0383	$\frac{c_p \nu_{inf} \rho_{inf}}{Pr}$ = 0.0539
$L_0 - L_z$	Re_x	$\delta^*(z = L_0) (m)$ (displacement thickness)	$\delta(z = L_0) (m)$ (boundary layer thickness)	
16.84 – 200 m	842-10,000	1	3	
$U_{ref} \left(\frac{m}{s} \right)$	$L_{ref} = \delta^* (m)$	$\nu_{ref} \left(\frac{m}{s^2} \right)$	$Re_{ref} = \frac{u_{ref} L_{ref}}{\nu_{ref}}$	
1.0	1.0	0.02	50	

$(L_x L_y L_z)^*$	$(n_x n_y n_z)$	grid stretching	
(200,60,4)	(128,96,4)	<ul style="list-style-type: none"> - Wall –normal hyperbolic ($\alpha = 2.75$) - Uniform grid in x, z 	
Inflow boundary	outflow boundary	freestream boundary	
$u = u_{blasius},$ $v = v_{blasius},$ $w = 0$ $T = T_{wall}$ (where the theoretical Blasius profiles are specified)	<i>Orlansky</i> $\frac{\partial \rho u_i}{\partial t} + U_c \frac{\partial \rho u_i}{\partial x_i} = 0$ $\frac{\partial \rho h}{\partial t} + U_c \frac{\partial \rho h}{\partial x_i} = 0$ $U_c = \frac{1}{L_y} \int u_{outflow} dy$	$\frac{du}{dy} = 0$ $\frac{dv}{dy} = 0$ $\frac{dw}{dy} = 0$ $\frac{dh}{dy} = 0$	<i>(Option)</i> $\frac{du}{dy} = 0, \frac{dw}{dy} = 0$ $v = v_{blasius}$ $\frac{dh}{dy} = 0$
wall boundary	Scalar Discretization Option	Periodicity	
$u = v = w = 0$ $T_{wall} = 450K$	QUICK	Spanwise	

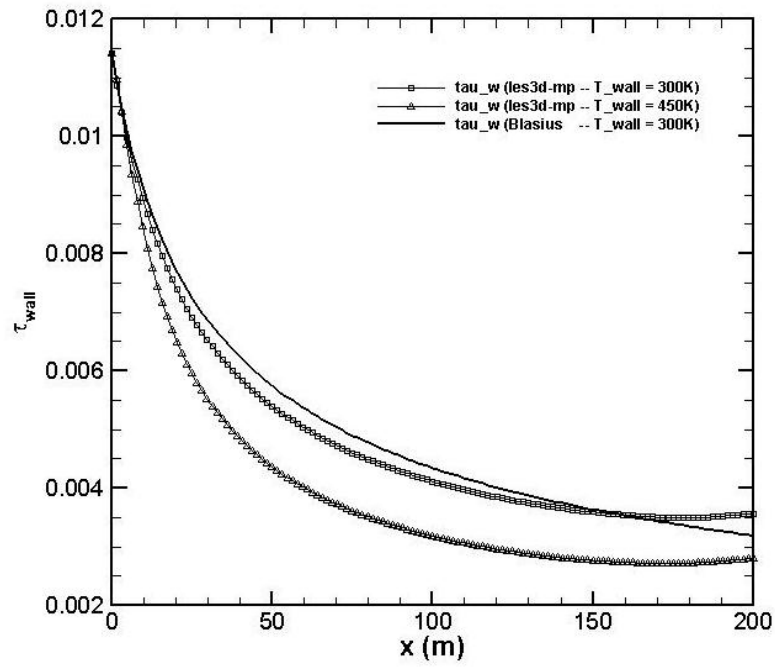
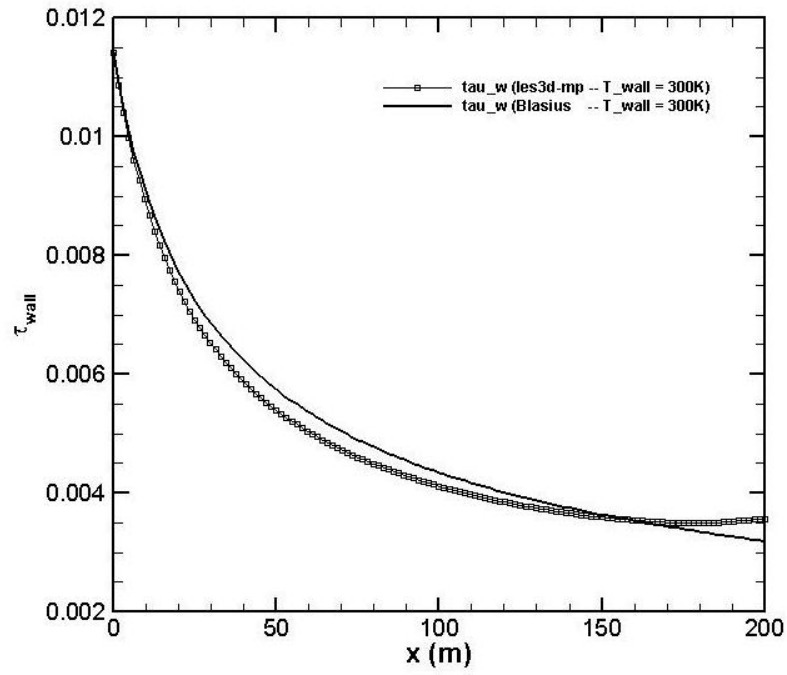


Figure 8. Blasius wall-shear stress no heat transfer (top), comparison to case with heat transfer and variable density (bottom).

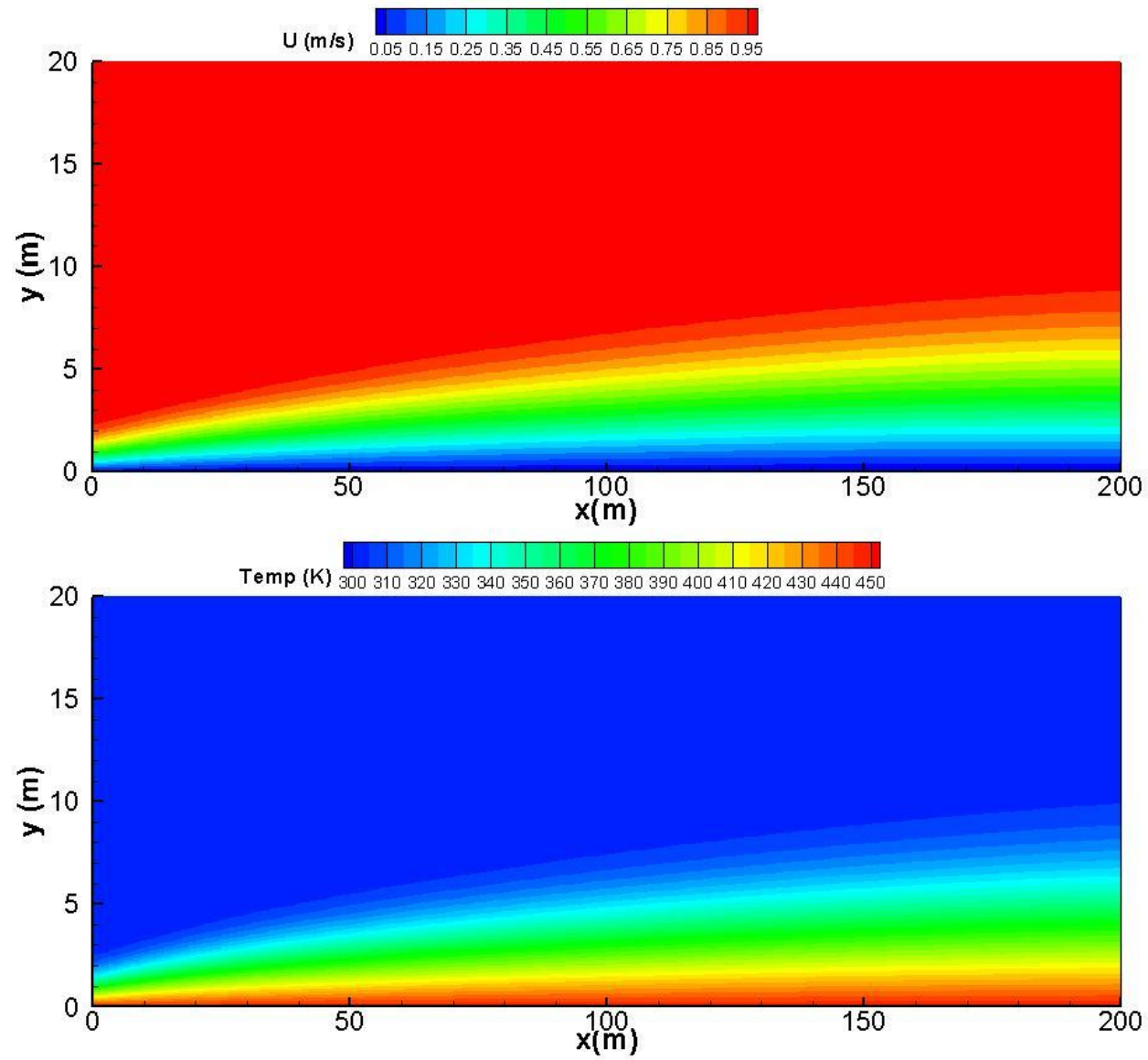


Figure 9. Velocity and temperature contours of Blasius case with variable density.

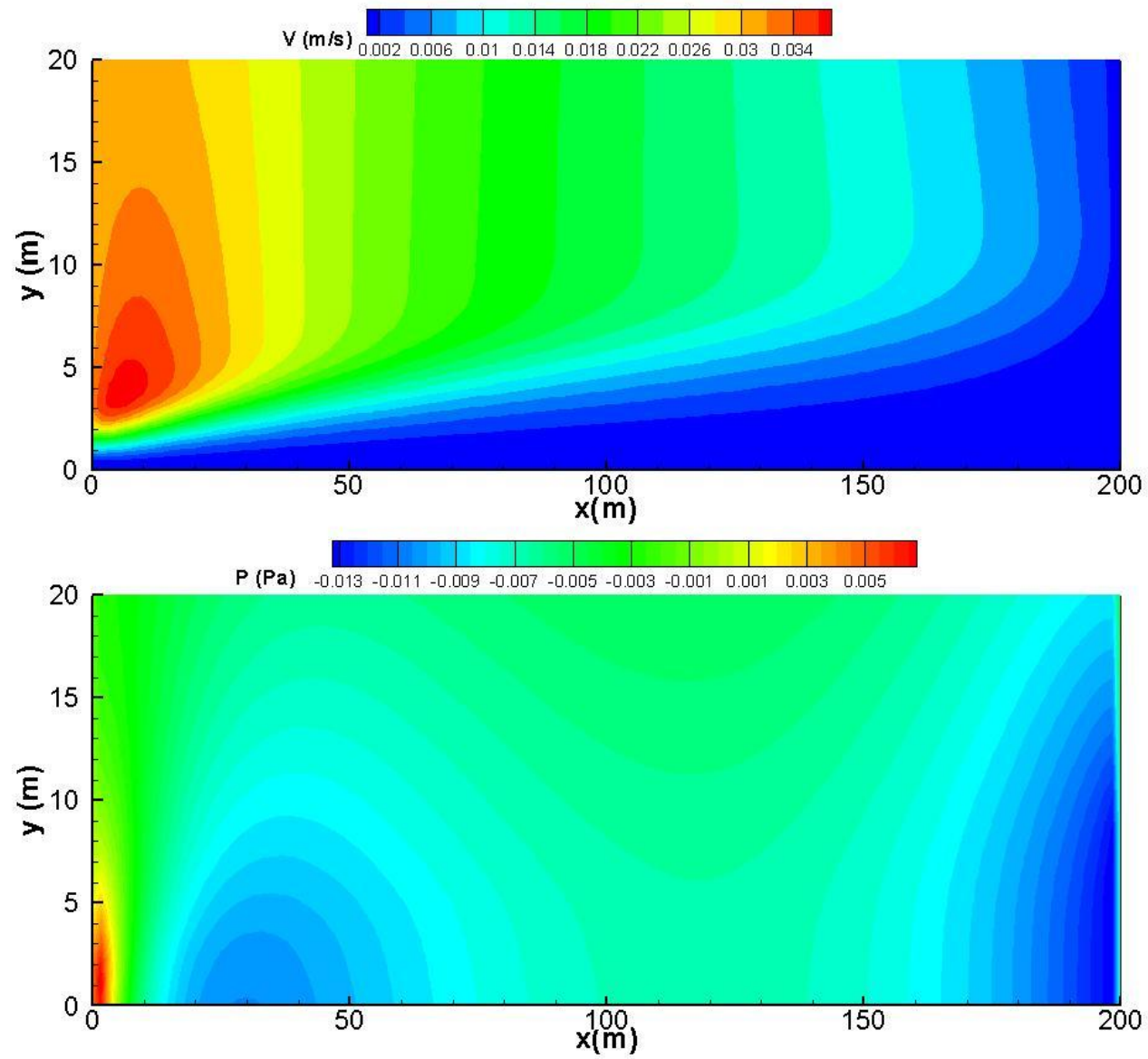


Figure 10. Lateral velocity and pressure contours of Blasius case with variable density

4.2 Natural convection boundary layer: Ostrach Solution

The solution of a laminar free convection boundary layer next to a heated isothermal plate was derived and developed by Ostrach [8]. This analysis presents a quasi-analytical solution to the problem based on similarity arguments and coupling between the temperature and velocity fields. This is an interesting test case for our purposes because it involves the modeling of a buoyancy driven boundary layer flow often found in applications involving fires. The modeling involves a vertical isothermal hot wall at 360K surrounded by an environment at 300K. That small temperature difference in temperature generates a laminar natural convection flow-structure in the fluid.

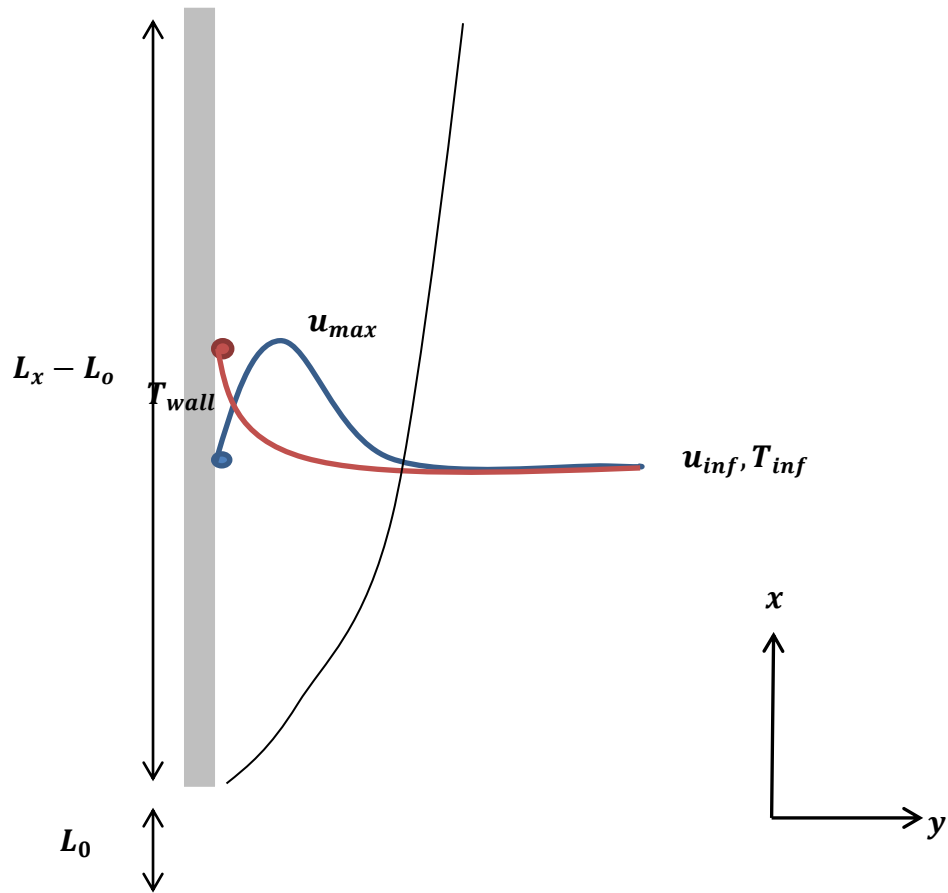


Figure 11. Free convection boundary layer schematic.

Testing parameters

$\nu_{inf}(m/s^2)$	$Pr = \frac{c_p \mu}{k}$	T_{wall}, T_{inf}	$\nu_{wall}(m/s^2)$	$k_{inf}(m/s^2)$
0.02	0.71	360K, 300K	$\nu_{inf} \left(\frac{T_w}{T_a} \right)^2 = 0.0288$	$\frac{c_p \nu_{inf} \rho_{inf}}{Pr} = 0.0281$
$L_x - L_0$	Gr_x	$\delta(x = 2m) (m)$	$U_{max}(x = 2m) \left(\frac{m}{s} \right)$	$U_{char}(x = 2m) (m/s)$
20.0m – 0.016m	5.5E + 01 – 6.9E + 04	1	1.1	$(g\beta\delta TL_z)^{0.5} = 1.97$
$U_{ref} \left(\frac{m}{s} \right)$	$L_{ref} (m)$	$\nu_{ref} \left(\frac{m}{s^2} \right)$	$Re_{ref} = \frac{u_{ref} L_{ref}}{\nu_{ref}}$	$Froude = g \left(\frac{L_{ref}}{U_{ref}^2} \right)$
1.1	2.0	0.02	110	16.2

$(L_x L_y L_z)^*$	$(n_x n_y n_z)$	grid stretching
(10,10,4)	(100,60,4) $\Delta y_{min} =$	<ul style="list-style-type: none"> - Wall –normal hyperbolic ($\alpha = 2.75$) - Uniform grid in x, z
Inflow boundary	outflow boundary	freestream boundary
$u = 0.05, T = T_{inf}$ $\frac{dv}{dx} = 0, \frac{dw}{dx} = 0$	<i>Orlansky</i> $\frac{\partial \rho u_i}{\partial t} + U_c \frac{\partial \rho u_i}{\partial x_i} - (\rho - \rho_\infty)g = 0$ $\frac{\partial \rho h}{\partial t} + U_c \frac{\partial \rho h}{\partial x_i} - (\rho - \rho_\infty)g = 0$ $U_c = \frac{1}{L_y} \int u_{outflow} dy$	$\frac{du_i}{dy} = 0$ $\frac{dh}{dy} = 0$
wall boundary	Scalar Discretization Option	Periodicity
$u = v = w = 0$ $T_{wall} = 360K$	QUICK	Spanwise

The table above presents the parameters used in running the test cases in les3d-mp. The simulation was performed for a larger than normal viscosity value of $\nu = 0.02m^2/s$. Due to the Grashof number dependence on the viscosity $Gr = g\delta T\beta L^3/\nu^2$ and its critical value needed for transition to turbulence ($Gr < 1.0 \times 10^7$) we can see that the effect of increasing the viscosity is also to increase the spatial region in the laminar regime. The set-up of this case in les3d-mp involved prescribing the temperature of the hot wall (360K) and allowing the flow to develop naturally. The reference values used in the run were taken at an elevation height of $L_x = 2.0 \text{ meters}$ defining the Reynolds and Froude number shown in table.

The simulation was run in lesd3-mp for a total of 500 time units, or 50 flow-through times defining a flow-through time as the time it takes for the inflow (1 m/s) to travel through the length of the domain. A good indication of the stability of the solution is a small magnitude of the peak pressure, since unphysical pressure surges will adversely influence the flow. The following figure shows minimum and maximum pressure perturbations with large values at initial times due to an adjusting of the flow.

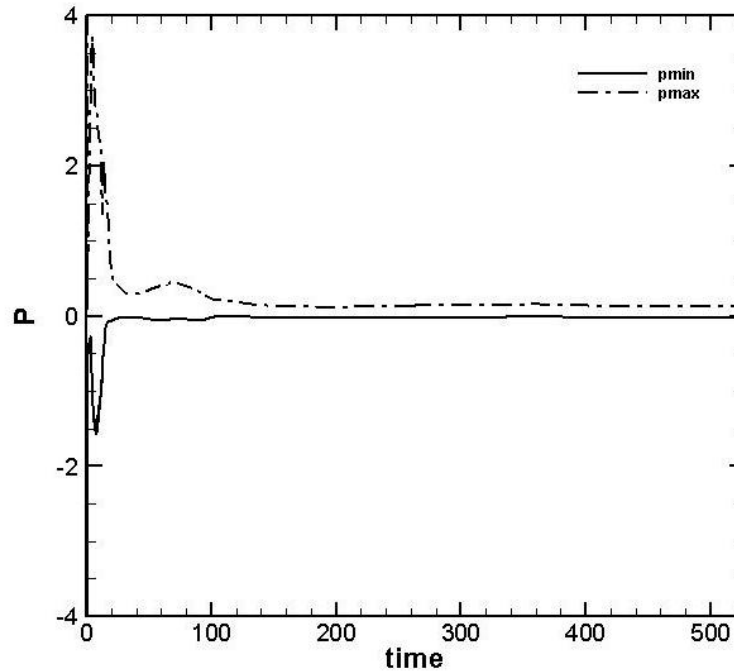


Figure 12. Time history of peak pressure.

Heat Flux

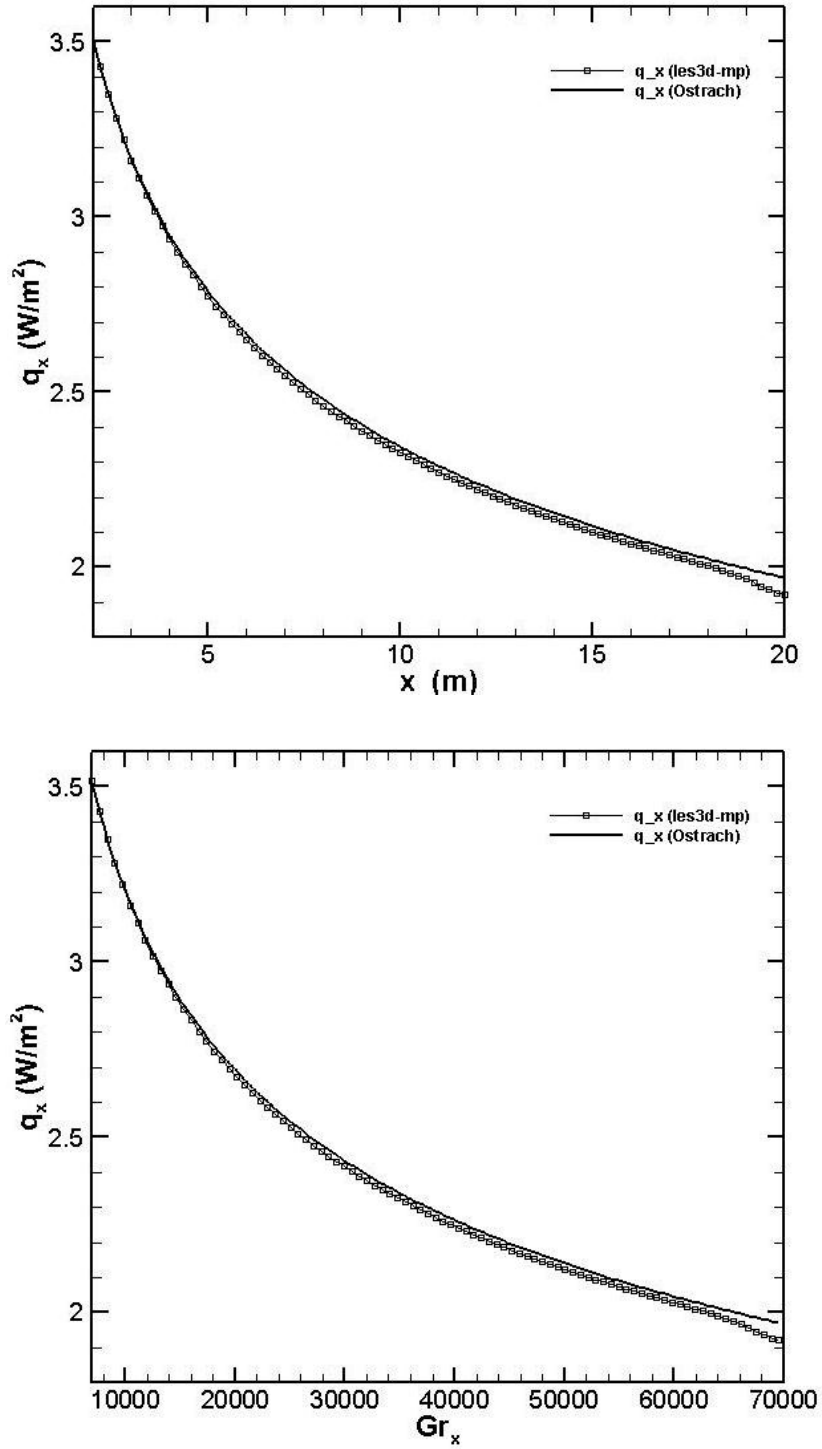


Figure 13. Heat flux comparison to Ostrach solution . Comparison with respect to plate elevation (top), comparison with respect to Grashof number (bottom).

Nusselt

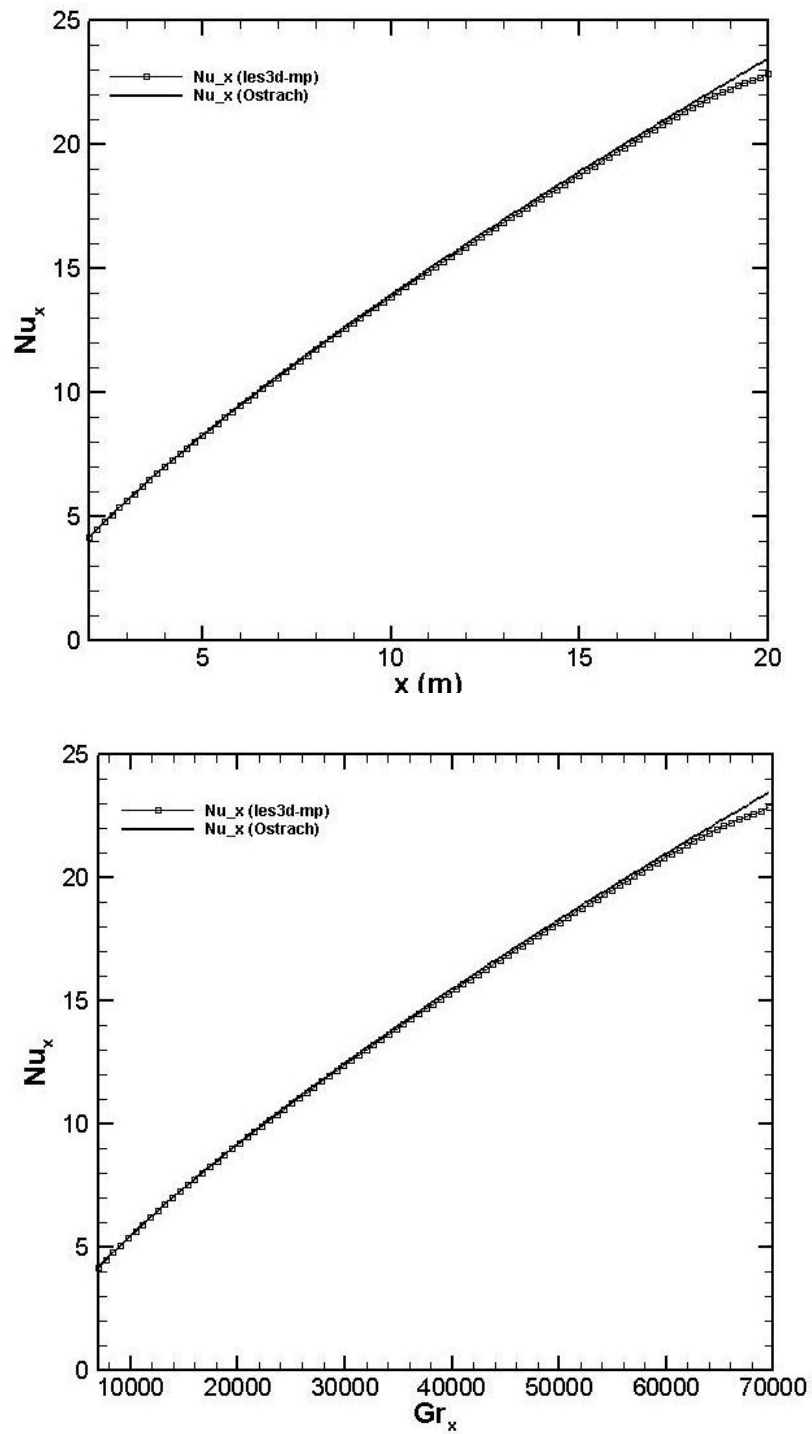


Figure 14. Nusselt number comparison to Ostrach solution . Comparison with respect to plate elevation (top), comparison with respect to Grashof number (bottom).

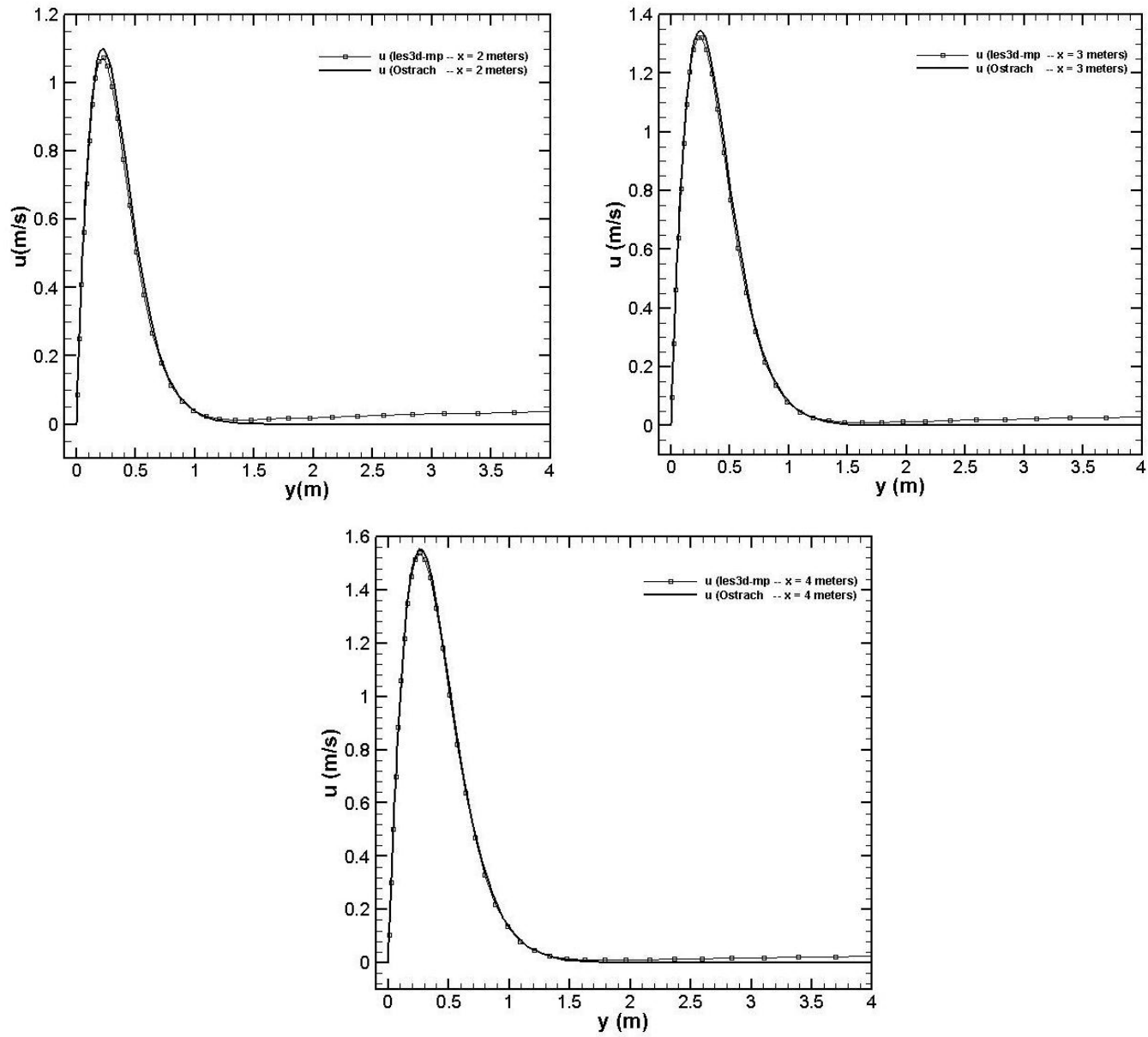


Figure 15. Velocity profiles at elevations $x=2$ m, 3 m, 3 m and compared to Ostrach.

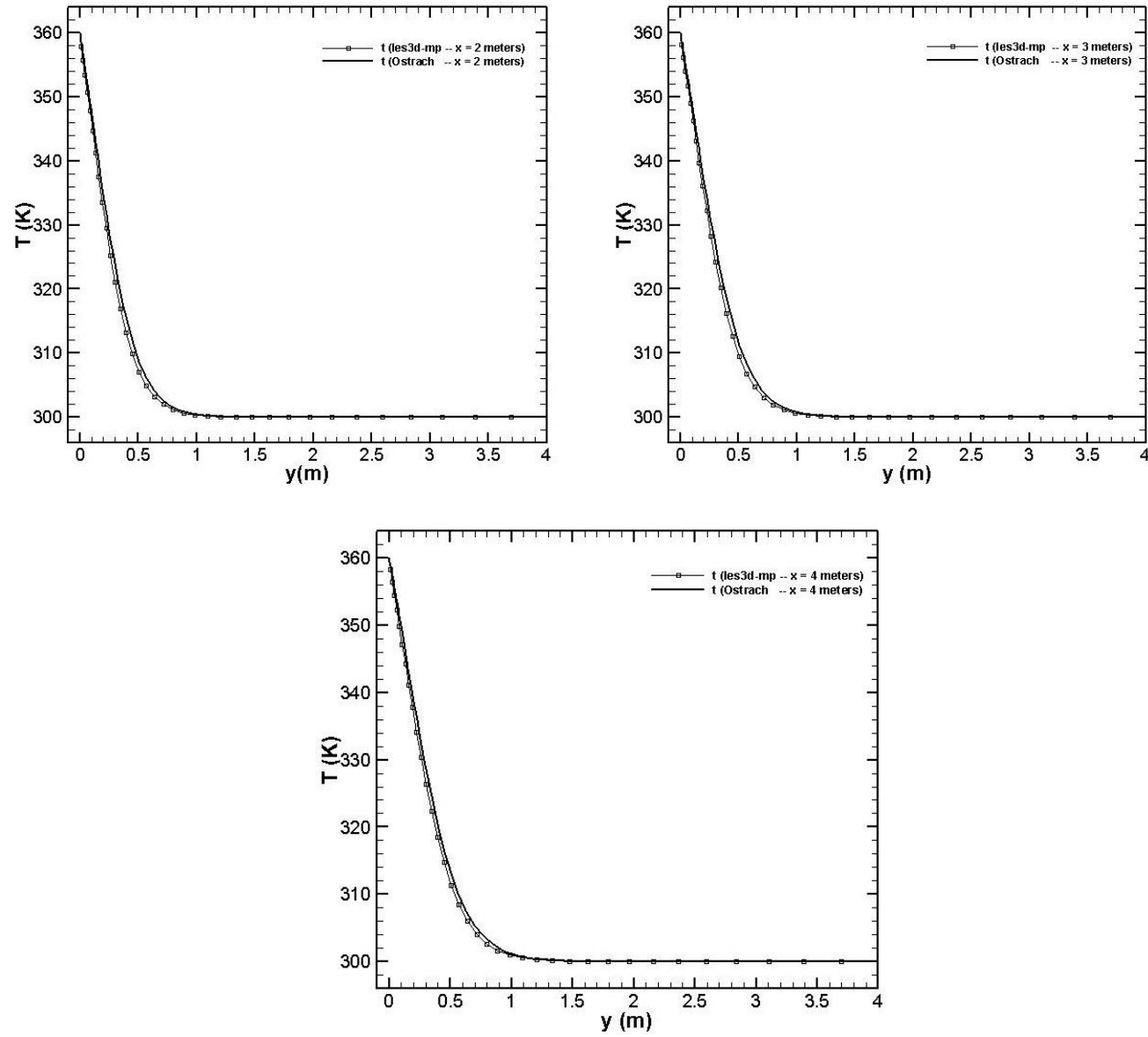


Figure 16. Temperature profiles at elevations $x= 2\text{m}, 3\text{m}, 3\text{ m}$ and compared to Ostrach.

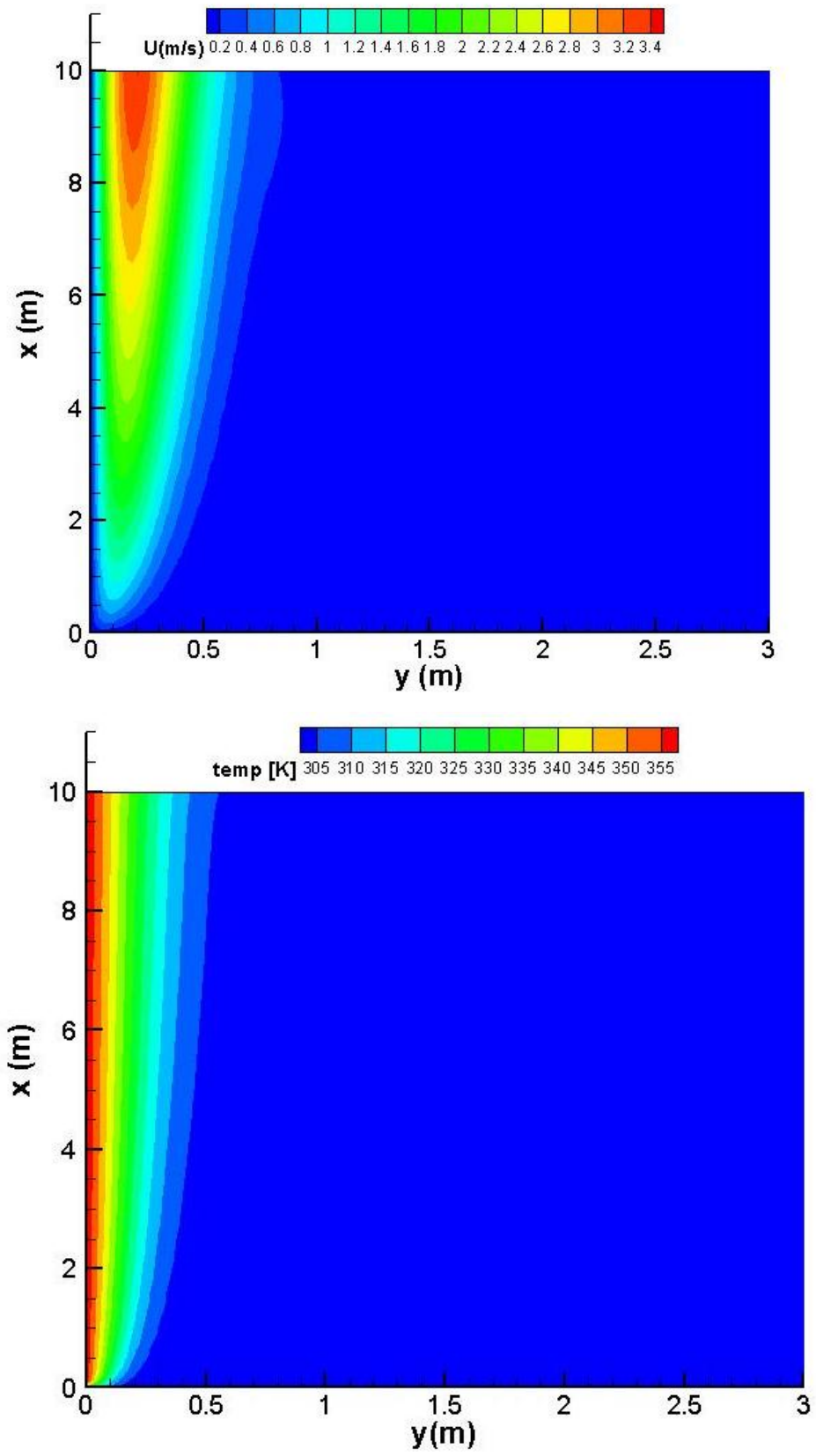


Figure 17. Natural convection velocity and temperature contours.

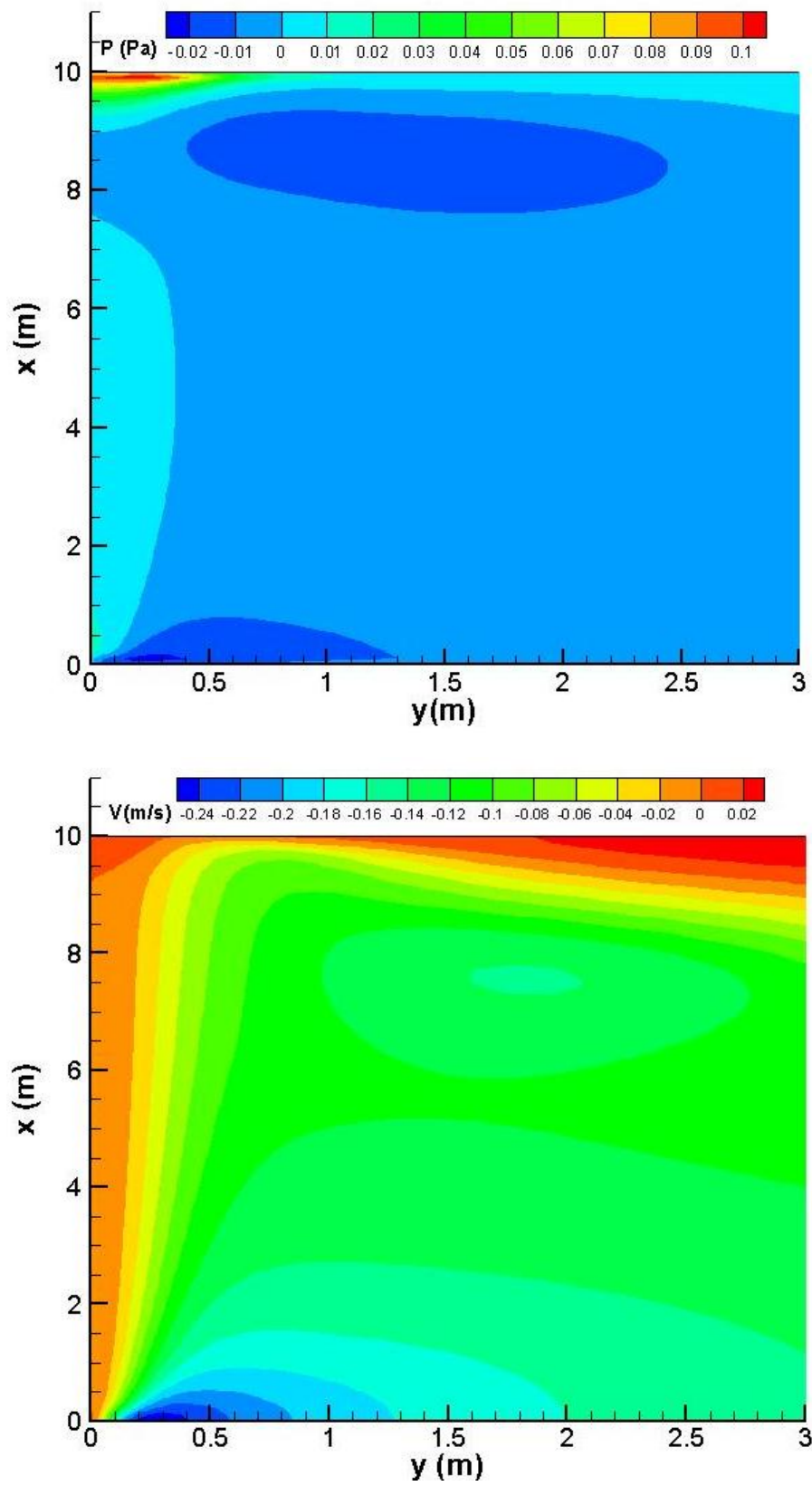


Figure 18. . Natural convection pressure and velocity contours

The results presented in figures 12-13 show good comparison to the theoretical Ostrach solution. The heat flux is presented as a function of elevation and the relative Grashof number showing the development of the solution. Similarly, Nusselt number results show close comparison to the analytical solution in both reference frames. Common to both numerical solutions is the slight deviation near the outflow. This occurs starting at ~ 18 meters to 20 meters and the peak deviation is less than 1 %. Although small this represents a problem in the outflow boundary conditions which can influence more sensitive diagnostics such as the entrainment velocity. This can be seen from the lateral velocity contours on figure 18.

Figures 15-16 show profiles of streamwise velocity and temperature at three reference stations. The reference stations are 2, 3 and 4 meters along the height of the plate. This shows good comparison to the Ostrach case inside the boundary layer thickness region with slight under-predictions of less than 2 %. Outside of the boundary layer region, the velocity profiles show the influence of a slight co-flow that was introduced at the inflow. The purpose of this is to introduce negligible streamwise velocity in regions where the flow approaches zero (such as the outside the boundary layer region) due to difficulties with Orlansky boundary conditions.

Reference

- [1] P. J. Roache, Verification and Validation in Computational Science and Engineering, Hermosa Publishers, Albuquerque NM, 1998.
- [2] “Guide for the Verification and Validation of Computational Fluid Dynamics Simulations,” AIAA G-077-1998.
- [3] Abanto, J., Pelletier, D., Garon, A., Trepanier, J. and Reggio, M., “Verification of some Commercial CFD Codes on Atypical CFD Problems,” AIAA-2005-682, 43rd AIAA Fluid Dynamics Conference and Exhibit, January 2005.
- [4] Kleb, B. and Wood, B., “CFD: A Castle in the Sand?,” AIAA-2004-2627, 36th AIAA Fluid Dynamics Conference and Exhibit, June 2004.
- [5] Roache, P. J., “Verification of Codes and Calculations,” *AIAA Journal*, Vol. 36, No. 5, May 1998, pp. 696-702.
- [6] Shunn, L., Ham, F., “Method of Manufactured Solutions Applied to Variable Density flow Solvers”, Center for Turbulence Research Annual Briefs, 2007, pg 155-168.
- [7] Orlansky, I; “A simple boundary condition for unbounded hyperbolic flows”, *Journal of Computational Physics*, **21**, 1976, pg 251.
- [8] Crawford, K; “Convective Heat and Mass Transfer”, Textbook.